Spatial-temporal changes of rainfall erosivity in the loess plateau, China: Changing patterns, causes and implications

Saiyan Liu[a], Shengzhi Huang[a,*], Yangyang Xie[b], Guoyong Leng[c], Qiang Huang[a], Lu Wang[a], Qi Xue[a,d]

[a] State Key Laboratory of Eco-hydraulics in Northwest Arid Region of China, Xi'an University of Technology, Xi'an 710048, China
[b] Yangzhou University, Yangzhou 225127, China
[c] Environmental Change Institute, University of Oxford, Oxford OX1 3QY, UK
[d] Yulin Municipal Water Affairs Bureau, Yulin 719000, China

ABSTRACT

Rainfall erosivity is one of the key factors influencing soil erosion by water. Improved knowledge of rainfall erosivity is critical for prediction of soil erosion and the implementation of soil and water conservation plan as well as sediment management projects under climate change. In this study, the Jing River Basin (JRB), a typical eco-environmentally vulnerable region of the Loess Plateau in China was selected as a case study. Spatial-temporal changing patterns of rainfall erosivity in the JRB were first examined, followed by detailed investigations of the underlying causes through exploring the relations among annual rainfall, large-scale atmospheric circulation patterns and rainfall erosivity using the cross wavelet technique. Furthermore, implications of changing rainfall erosivity for sediment load and vegetation cover were analyzed. Results indicated that: (1) the year 1985 was a turning point in the time series of annual rainfall erosivity, demonstrating the non-stationary feature. Seasonal rainfall erosivity showed a spatial gradient with decrease from the upper to the lower stream. Rainfall erosivity was the largest in summer, and has increased significantly in the eastern basin; (2) annual rainfall erosivity showed a strong positive correlation with annual rainfall amount, implying that decrease of rainfall may have led to the reduction of rainfall erosivity in recent decades; (3) El Niño-Southern Oscillation and Pacific Decadal Oscillation were correlated with rainfall erosivity during 1982–1991, suggesting that large-scale atmospheric circulation patterns have strong influences on the changing patterns of rainfall erosivity; (4) changing rainfall erosivity had negligible impacts on the variation of vegetation cover (as indexed by the Normalized Differential Vegetation Index), but has detectable influence on sediment discharge which was further modulated by local soil and water conservation practice since the 1970s. These findings are helpful for prediction of soil erosion and adaptation strategies through local soil erosion control measures and sediment control projects.

1. Introduction

Soil erosion by rainfall is a severe ecological and agricultural concern, with large impacts on social and economic development worldwide by reducing agricultural productivity and increasing the risk of landslide activity (Panagos et al., 2015) and eco-environment deterioration (Lee and Heo, 2011). Furthermore, transportation of eroded particles through runoff could favor the deposition of sediment, resulting in loss of reservoir storage (Jebari et al., 2012). Therefore, accurate prediction and evaluation of soil erosion is of great importance for soil erosion control and sediment management (Lee and Heo, 2011). The Universal Soil Loss Equation (USLE) (Wischmeier and Smith, 1978)

and its revised version RUSLE (Renard et al., 1997) have been the most widely used empirical models for assessing and predicting soil erosions by water. In these models, soil loss is a function of rainfall erosivity (R factor), soil erodibility (K factor), slope length (L factor) and steepness (S factor), cover (C factor) and conservation practices (P factor). Among these factors, rainfall erosivity, defined as the potential capability of rainfall to erode soil, is recognized as the key factor influencing soil erosion by water (Hoyos et al., 2005; Lee and Heo, 2011; Panagos et al., 2015; Ballabio et al., 2017).

Understanding the change patterns of rainfall erosivity expressed in terms of rainfall amount and intensity (Hoyos et al., 2005) is critical for soil erosion modeling, soil and water conservation planning, soil loss

recurrence analysis (Xie et al., 2016), sediment management, water quality modeling (Lee and Heo, 2011), non-point source pollution assessment (Xie et al., 2016), landslide and flood risk assessment (Panagos et al., 2015) and agricultural management (Maracchi et al., 2005). Under a changing climate, terrestrial hydrological cycle has accelerated (Trenberth, 2011) with more frequent extreme rainfall (Santos et al., 2011; IPCC, 2013; Huang et al., 2015a, 2015b; Liu et al., 2017; Fang et al., 2017). Extreme rainfall, especially those rainfall events with strong intensity and short duration, tend to be more erosive (Wei et al., 2007; Huang et al., 2016a, 2016b, 2016c; Fang et al., 2018; Huang et al., 2018). Therefore, improved knowledge of the changing characteristics of soil erosion is important for making soil conservation and sediment control strategies.

Recently, evaluation of rainfall erosivity has been well documented in the literature (Ramos and Durán, 2014). For example, Panagos et al. (2015) investigated the changes in annual rainfall erosivity in Europe and identified Mediterranean and Alpine as vulnerable regions where thunderstorms have become more frequent than in other areas. Ballabio et al. (2017) presented a study on monthly rainfall erosivity and found an increasing tendency of erosivity during the winter and summer seasons in Western and Eastern parts of Europe. Vrieling et al. (2010) showed that the highest erosivity in Africa was distributed along the west coast and northern half of Madagascar. At regional scale, Hoyos et al. (2005) revealed remarkable differences in rainfall erosivity between wet and dry seasons in Colombian Andes. Borrelli et al. (2016) investigated the spatio-temporal distribution of rainfall erosivity in Italy based on a gridded map of rainfall erosivity. Oliveira et al. (2012) found that rainfall erosivity in Brazil has a spatial gradient with increase from east to west, and the lowest and highest rainfall erosivity were located in the northeast and north parts of the country, respectively. Mello et al. (2015) compared the performance of regression-kriging method for R factor prediction with other methods, and demonstrated its greater prediction accuracy for developing R factor maps for Brazil. Based on 270 years of data, Bonilla and Vidal (2011) found an increasing trend in rainfall erosivity in central Chile. Angulo-Martínez and Beguería (2009) showed distinct spatial and seasonal patterns of rainfall erosivity in the Ebro Basin, Northeastern Spain. In China, an increasing trend of annual erosivity was observed in the arid zone, while a decreasing trend was found in the sub-humid zone, and no evident trends were detected in the semi-arid zone (Yang and Lu, 2015). Recently, increasing trends of spring and winter rainfall erosivity have been reported in the Yunnan Plateau, Southwest China (Gu et al., 2016). Previous studies have well advanced our knowledge of changing patterns of rainfall erosivity under the background of climate change, which showed that rainfall erosivity mainly depended on precipitation seasonality, temperature and other bioclimatic factors (Panagos et al., 2015; Ballabio et al., 2017).

It has been well demonstrated that large-scale atmospheric circulation patterns, including El Niño–Southern Oscillation (ENSO) and Pacific Decadal Oscillation (PDO), are responsible for the spatial and temporal variability of rainfall (Croitoru et al., 2015; Limsakul and Singhruck, 2016; Liu et al., 2018). Given the fact that rainfall erosivity is closely linked with rainfall pattern (Panagos et al., 2015), investigation of the teleconnection between atmospheric circulation patterns and regional rainfall erosivity would thus shed light on the mechanism behind the changes in rainfall erosivity. To date, limited studies have been conducted in this regard. Angulo-Martínez and Beguería (2012) found that rainfall erosivity became stronger during the negative phases of North Atlantic Oscillation (NAO), the Mediterranean Oscillation (MO) and the Western Mediterranean Oscillation (WeMO) in Northeastern Spain. However, their analysis was mainly based on the rank test, which can only reveal general relationships between atmospheric circulation patterns and rainfall erosivity. A more advanced approach such as the cross wavelet analysis is required to explore the correlations in both time and frequency fields (Huang et al., 2015a), which is of important significance for prediction of soil erosion.

Besides its effects on soil erosion, rainfall erosivity may exert impacts on plant growth. Djebou et al. (2015) found that vegetation coverage variation was closely related to the variability of rainfall. Significant correlation between rainfall and NDVI (normalized difference vegetation index) have also been observed worldwide (Li et al., 2003; ChamailléJammes and Fritz, 2009; He, 2014). Although previous studies have enhanced our understandings on the relationship between rainfall magnitude and vegetation coverage, the effect of rainfall erosivity on vegetation cover has not been well demonstrated. Indeed, landslides, floods and soil erosion could effectively change vegetation structure and composition for long time periods at large scale (Sun et al., 2013). Hence, knowledge of vegetation coverage response to changing rainfall erosivity can help guide soil conservation practices.

Loess Plateau in China is featured with highly erodible loess layers. Centuries of unsustainable farming practices and huge population growth have led to severe environmental degradations in the Loess Plateau. The susceptibility of Loess Plateau to soil erosion hazard is found to be mostly influenced by a few erosive rainfall events that are short and intense (Xin et al., 2011). Previous studies have well examined the long-term trend of annual erosive rainfall and annual rainfall erosivity in the study region (Xin et al., 2011; Yue et al., 2014), but few have explored the implications of rainfall erosivity on vegetation coverage and sediment load variations, which have great implications for local soil and water conservation, sediment management and ecological restoration.

The main objectives of this study are: (1) to examine the changing patterns of rainfall erosivity in a river basin in the Loess Plateau, and assess whether its stationarity is valid or not; (2) to explore the possible causes of rainfall erosivity variation from the perspective of local-scale and large-scale climate changes; (3) to investigate the impacts of changing rainfall erosivity on the variations of local vegetation coverage and sediment load.

2. Study area and data

2.1. Study area

The Jing River Basin (JRB) located in the central part of the Loess Plateau (106.2°E–109.1°, 34.8°N–37.4°N), was selected as the study region. It is the secondary tributary of the Yellow River Basin (YRB) and the largest tributary of the Wei River Basin (WRB) in China (Fig. 1). The drainage area of JRB is 45,400 km^2, directly supporting a population of 6 million. Mean annual rainfall is approximately 545 mm with nearly 60% concentrated in summer (from June to August). Loessial soil and dark loessial soil are the typical soil types across the basin, which are highly erodible. Forest coverage rate in the basin is only about 6.5%.

Extensive rainfalls in summer combined with the erosion-prone soils, steep landscapes and low vegetation coverage make JRB one of the most sediment-laden tributaries of the YRB. It was recorded that annual average sediment transported into the JRB is approximately 2.6×10^8 t, accounting for nearly 14% of sediment load of the YRB (Xin et al., 2011). In order to reduce soil loss, a series of conservation measures including Grain for Green Projects have been implemented since 1970s (Xin et al., 2011), which have greatly improved vegetation cover, leading to changes in surface hydrology (Li et al., 2009).

There are nine meteorological stations (Fig. 1 and Table 1) in the study region. Detailed information of these stations is provided in Table 1. In addition, there is a hydrological station Zhangjiashan in the lower reaches of the JRB, which controls the whole basin.

2.2. Data

Daily rainfall data (1960–2010) obtained from the National Climate Center (NCC) of the China Meteorological Administration (CMA) were analyzed in this study. To examine the relationship between rainfall erosivity and large-scale atmospheric circulations, correlations between
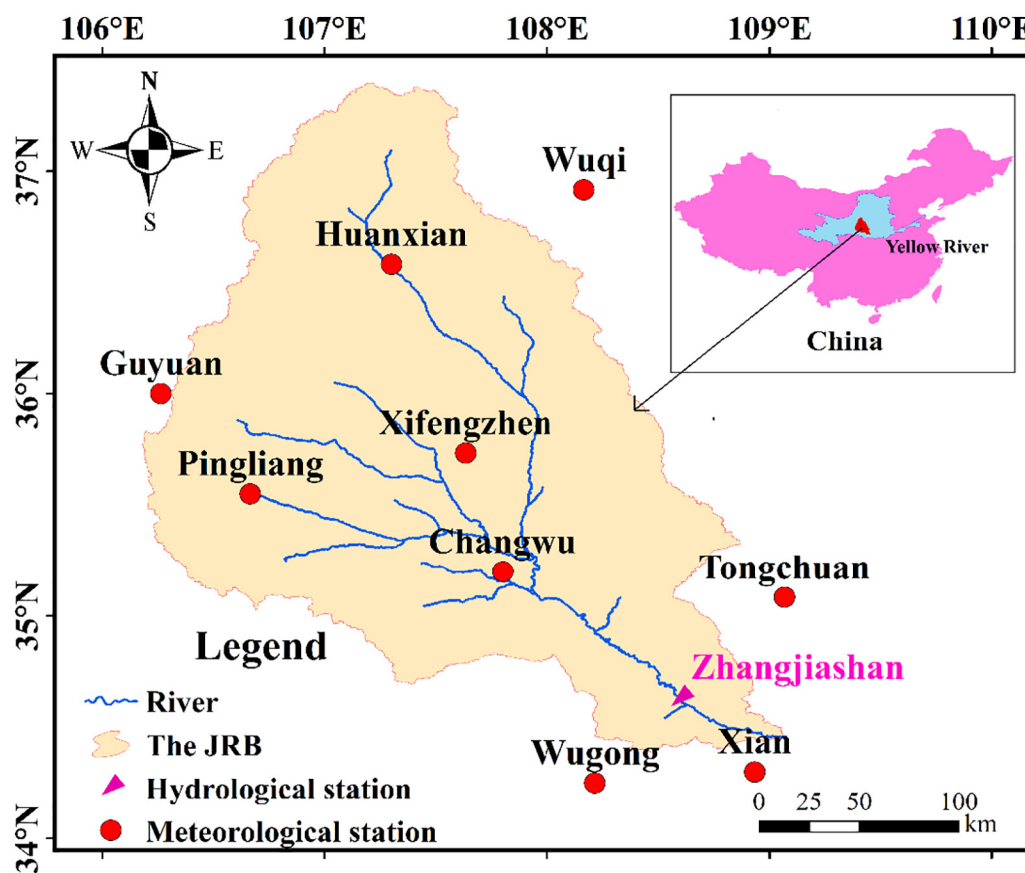
Fig. 1. Study area and relevant meteorological/hydrological stations.

rainfall erosivity and the ENSO and PDO indices were investigated. The Multivariate ENSO Index (MEI) is used to characterize the state of ENSO events since it integrates more information for monitoring the ENSO phenomenon than other indices (Limsakul and Singhruck, 2016). MEI data are freely available at http://www.esrl.noaa.gov/psd/enso/mei/table.html. Monthly PDO index (PDOI), which is defined as the leading principal component of North Pacific monthly sea surface temperature variability, was obtained from http://research.jisao.washington.edu/pdo/PDO.latest.txt. Normalized Differential Vegetation Index (NDVI) data (1982–2010), stemming from the Land Processes Distributed Active Archive Center (DAAC) of National Aeronautics and Space Administration (NASA) (https://lpdaac.usgs.gov/), were used to explore vegetation coverage response to the changing patterns of rainfall erosivity. Furthermore, annual sediment load data (1960–2010) from the Yellow River Conservancy Commission (YRCC) were collected to study the impacts of changing rainfall erosivity on sediment load.

3. Methodology

3.1. Calculation of rainfall erosivity

In this study, erosive rainfall is defined as the day with rainfall amount larger than or equal to 12.0 mm (Xin et al., 2011). Rainfall erosivity can also be estimated based on the EI30 index, which requires high temporal resolution rainfall data (< 60 min) that is not easily accessible (Panagos et al., 2015). As an alternative, many attempts have been made to estimate rainfall erosivity using annual, monthly and daily rainfall data. Through comparative analysis, it was shown that daily rainfall data could be used to predict rainfall erosivity accurately (Angulo-Martínez and Beguería, 2009; Gu et al., 2016; Xie et al., 2016). Hence, in this study, rainfall erosivity was calculated based on daily rainfall data following the method of Zhang et al. (2002), which has been widely adopted in the First National Water and Soil Conservation Survey in China.

Table 1
The information of weather stations in the JRB.

Station	Latitude (N)	Longitude (E)	Altitude (m)	Rainfall amount (mm)	Rainfall erosivity (MJ·mm·ha^{-1}·h^{-1}·a^{-1})
Changwu	35.20	107.80	1206	446	2302
Guyuan	36.00	106.27	1753	425	1315
Huanxian	36.58	107.30	1255	499	1304
Pingliang	35.55	106.67	1346	783	1697
Tongchuan	35.08	109.07	978	466	3761
Wugong	34.25	108.22	447	596	2606
Wuqi	36.92	108.17	1331	565	1643
Xian	34.30	108.93	397	546	2332
Xifengzhen	35.73	107.63	1421	580	2098

Note: "Rainfall amount" and "Rainfall erosivity" denote the mean annual rainfall amount and the mean annual rainfall erosivity, respectively.

The formula for calculation is as follows:

$$R_{ik} = \alpha \sum_{j=1}^{M} P_{d_{ikj}}{}^{\beta} \tag{1}$$

$$\alpha = 21.239\beta^{-7.3967} \tag{2}$$

$$\beta = 0.6243 + \frac{27.346}{\overline{P_{d_0}}} \tag{3}$$

$$\overline{P_{d_0}} = \frac{1}{N} \sum_{i=1}^{N} \sum_{k=1}^{12} \sum_{j=1}^{M} P_{d_{ikj}} \tag{4}$$

$$R_i = \sum_{k=1}^{12} R_{ik} \tag{5}$$

where R_{ik} is rainfall erosivity in the k-th month of the i-th year (MJ·mm·ha^{-1}·h^{-1}); N denotes the length of the data (years); M is the number of erosive rainfall in the k-th month of the i-th year; $P_{d_{ikj}}$ represents the amount of erosive rainfall in the k-th months of the i-th year; α and β stand for the undetermined parameters, respectively; $\overline{P_{d_0}}$ is the annual average of erosive rainfall; R_i denotes the annual rainfall erosion in the i-th year (MJ·mm·ha^{-1}·h^{-1}), which is referred to as annual rainfall erosivity for simplicity.

3.2. Modified Mann-Kendall trend test

Original Mann-Kendall (MK) test is a commonly used non-parametric test technique for estimating change trends in time series (Mann, 1945; Kendall, 1955). It is distribution free and performs well for non-normally distributed and censored data. However, the presence of serial correlations in time series may result in unreliable results. Therefore, the modified Mann-Kendall (MMK) test was proposed to remove the impact of the autocorrelation, which was proven robust in studying the trends of hydro-meteorological time series (Hamed and Rao, 1998; Daufresne et al., 2009).

The standardized test statistic (Z) of trend test is computed as

$$Z = \frac{S}{\sqrt{Var(S)}} \tag{6}$$

where S is the MK trend test statistic; and $Var(S)$ is the variance of S.

Considering the influence of autocorrelation of time series, the MMK test calculates $Var(S)$ as

$$Var_1(S) = Var_0(S)\left[1 + \frac{2}{n(n-1)(n-2)}\sum_{i=1}^{n-1}(n-1)(n-i-1)(n-i-2)\rho_S(i)\right] \tag{7}$$

where $Var_1(S)$ and $Var_0(S)$ represent the $Var(S)$s in MMK test and MK test, respectively; n is the length of given time series; $\rho_S(i)$ is the autocorrelation coefficient of given time series at lag i; and more details about the MMK test could be referred to Huang et al. (2014).

In this study, the MMK test was applied to estimate the change trends in rainfall, rainfall erosivity, sediment load and NDVI at the 95% significance level.

3.3. Heuristic segmentation method

Climatic system is characterized with nonlinear, non-stationary and hierarchical features, making traditional statistical method such as the sliding T/F test, Mann-Kendell test and rank sum test hard to identify and analyze abrupt changes reasonably (Huang et al., 2014). By contrast, the heuristic segmentation algorithm proposed by Bernaola-Galván et al. (2001) is well fitted to nonlinear and non-stationary time series (Huang et al., 2014).

A sliding pointer is first set for a given time series $X = x_1, x_2, ..., x_n$, and then moves from x_1 to x_{n-1} one by one. n is the length of X. Thus,

the pointer divides X into two subseries with one on the left and the other right of the pointer. The mean and standard deviations of the two subseries are then calculated. The difference in their means (i.e. x_{avg}^L and x_{avg}^R) is estimated as

$$T(i) = \left| \frac{x_{avg}^L(i) - x_{avg}^L(i)}{s(i)} \right| \tag{8}$$

$$s(i) = \sqrt{\frac{(n^L - 1) \cdot s^L + (n^R - 1) \cdot s^R}{n - 2} \times \left(\frac{1}{n^L} + \frac{1}{n^R}\right)} \tag{9}$$

where $T(i)$ is the statistic representing the difference in mean values when the pointer reaches the position i ($1 \le i < n$), following the student-t distribution; $s(i)$ is the pooled variance at the position i; and n^L (n^R) is the length of left (right) subseries, where $n^L + n^R = n$.

In Eq. (8), $T(i)$ is a function of the position (i) of pointer in X. The pointer's position corresponding to the largest T value is taken as a candidate of change point. Then, the statistical significance $P(t_{max})$ corresponding to the largest T is approximated as follows:

$$P(t_{max}) \approx \{1 - I_{[\nu/(\nu + t_{max}^2)]}(\delta\nu, \delta)\}^{\eta} \tag{10}$$

where $\eta = 4.19 \ln(n) - 11.54$ and $\delta = 0.40$, in which η and δ are obtained by means of the Monte Carlo simulations; $\nu = n - 2$, and $I_x(a, b)$ is the incomplete beta function.

If $P(t_{max})$ is smaller than a threshold of P_0 (typically set to 0.95), the time series will not be split. Otherwise, the time series will be cut into two subseries, and the iteration of the above procedure on each new subseries continues until $P(t_{max}) < P_0$ or the length of the acquired subseries is shorter than the presupposed minimum segment length l_0 ($l_0 = 25$).

3.4. The cross wavelet analysis

The cross wavelet analysis, based on the wavelet transform and cross spectrum analysis, is designed to examine the linkage between two time series in a comprehensive way compared to traditional methods (such as Fourier transform). Specially, it can not only detect the correlations between two time series, but also reflect their phase structure and local characteristics in both time and frequency domains (Hudgins et al., 1993; Torrence and Compo, 2010; Shao, 2013; Huang et al., 2015a). Since rainfall erosivity is highly variable and probably non-stationary, a better understanding of the potential driving forces could be gained through the cross wavelet analysis.

More details on the theory and calculation process can be referred to Torrence and Compo (2010) and Labat (2010), and related codes are available freely at http://noc.ac.uk/using-science/crosswavelet-wavelet-coherence.

4. Results and discussion

4.1. Changing patterns of rainfall erosivity

4.1.1. Changes of annual rainfall erosivity

The long-term mean annual rainfall erosivity in the JRB during 1960–2010 is 2117.70 MJ·mm·ha^{-1}·h^{-1}, with a high standard deviation of 401.8 MJ·mm·ha^{-1}·h^{-1}. The lowest rainfall erosivity of 1422.6 MJ·mm·ha^{-1}·h^{-1} occurred in the year 1997, while the highest rainfall erosivity of 3177.1 MJ·mm·ha^{-1}·h^{-1} was in 1983. The spatial distribution of annual rainfall erosivity is presented in Fig. 2A. It can be observed from Fig. 2A that rainfall erosivity showed an evident spatial gradient across the basin, which increases from north to south. The largest rainfall erosivity was in the downstream of the JRB, while the lowest rainfall erosivity mainly occurred in the upstream of the JRB (Fig. 2A). This calls for effective measures to prevent soil erosion, as there are widespread cultivated lands in the Guanzhong Plain in the downstream (Qi et al., 2009).
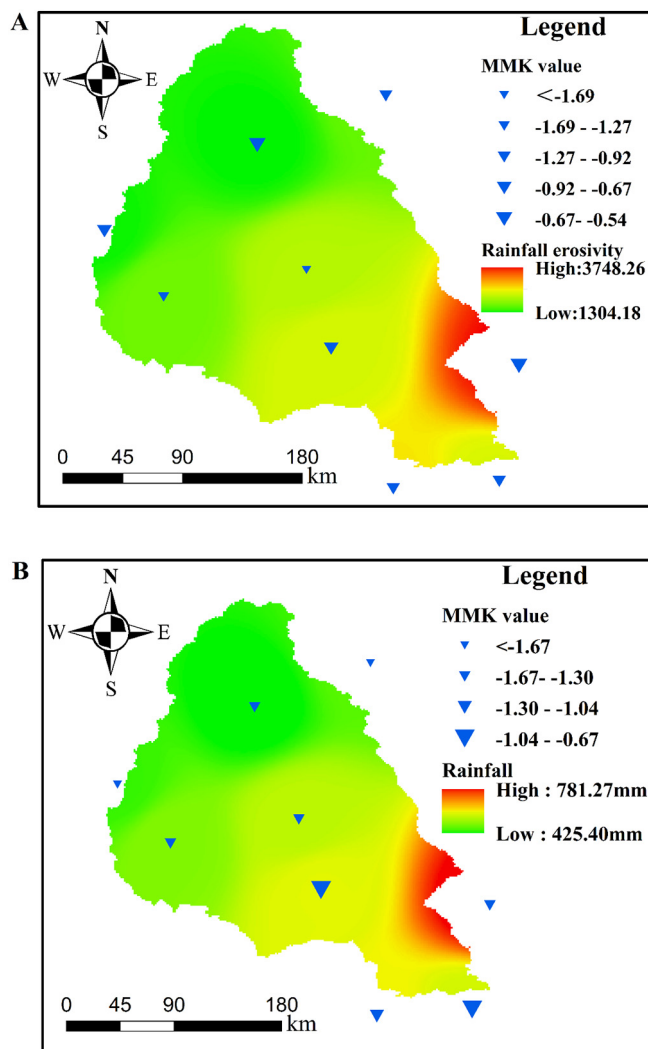
Fig. 2. The spatial distribution of annual average rainfall erosivity/rainfall and trends over the JRB: (A) rainfall erosivity (unit: MJ·mm·ha^{-1}·h^{-1}·a^{-1}); (B) rainfall.

Fig. 2A also shows the spatial distribution of changing trends of annual rainfall erosivity across the basin. It is found that the JRB was dominated by insignificant decreasing trends of rainfall erosivity with statistic values larger than −1.96 but < 0. The range of rainfall

erosivity of the JRB was similar to that observed in other temperate climate regions, such as Slovenia (where rainfall erosivity ranges from 1318 MJ·mm·ha^{-1}·h^{-1} to 2995 MJ·mm·ha^{-1}·h^{-1}) (Oliveira et al., 2012). These results are also in agreement with previous studies (Xin et al., 2011; Yang and Lu, 2015; Qin et al., 2016) showing a reduction of soil erosion risk across the Loess Plateau to some extent.

4.1.2. Changes of monthly and seasonal rainfall erosivity

Spatial distribution of monthly rainfall erosivity is broadly similar to that of corresponding rainfall amount. In general, rainfall erosivity has exhibited a large seasonal variability, with the lowest long-term mean value of 4.9 MJ·mm·ha^{-1}·h^{-1} in December and the maximum value of 534.2 MJ·mm·ha^{-1}·h^{-1} in July. MMK trend test results for monthly rainfall erosivity are summarized in Table 2.

As shown in Table 2, a decreasing trend of rainfall erosivity can be found in spring (from March to May), especially in the eastern part of the JRB. At Wugong and Xi'an stations, the rainfall erosivity change trends in April are statistically significant at the 95% confidence level with statistic values less than −1.96. During the summer season (from June to August), a positive change trend was observed in one third stations. In the eastern basin, the increasing trends were significant in June and August. Besides, significant decreasing trends were detected in one third of stations in the northeast part of the JRB in autumn (from September to November). Overall, no significant trends of rainfall erosivity were observed in winter (from December to January) across the basin. Given the increasing trend of rainfall erosivity in summer, it is possible that risk of local soil and water loss and landslide activity may have aggravated across the basin. Hence, sustainable soil conservative practices should be taken in advance (Panagos et al., 2015).

The spatial distribution of seasonal mean rainfall erosivity is shown in Fig. 3. Similar spatial distribution patterns are observed among spring, summer and autumn seasons. In general, seasonal mean rainfall erosivity gradually decreased from the upper to the lower stream of JRB. The largest seasonal mean rainfall erosivity occurred in summer followed by autumn, spring and winter, accounting for 54% of annual mean rainfall erosivity. Mean rainfall erosivity in summer was smaller in the middle stream than that in the upper and lower streams of the JRB, inconsistent with the patterns observed in other three seasons. Relatively, the mean rainfall erosivity in winter is negligible compared with that in other seasons.

4.1.3. The change point of annual rainfall erosivity

As outlined in Section 4.1.1, annual rainfall erosivity in the JRB has exhibited nonlinear and non-stationary features. Here, the heuristic segmentation method introduced in Section 3.3 was applied to identify the change points of annual rainfall erosivity. Fig. 4 presents the

Table 2
The modified Mann-Kendell test statistics of monthly rainfall erosivity in each month at each station in the JRB.

Month	Meteorological stations ranking from west to east in the JRB								
	GY	PL	HX	XF	CW	WQ	WG	XA	TC
Jan	0.0	−0.3	0.0	−0.3	−0.3	−0.3	−0.3	−0.3	−0.3
Feb	0.0	−0.3	0.1	0.0	−0.3	0.0	−0.1	−0.3	0.3
Mar	0.1	−0.5	0.0	−0.2	−0.4	−0.2	0.4	−0.7	0.3
Apr	−0.9	−1.7	0.7	−1.6	__−2.4__	−1.3	__−3.0__	__−2.3__	__−3.3__
May	−0.2	−0.1	−0.9	−0.5	−0.2	0.1	−1.6	__−2.5__	0.4
Jun	0.4	0.4	1.5	0.8	**2.5**	0.7	**2.5**	1.3	0.8
Jul	−0.4	−0.1	0.0	0.7	0.3	−0.1	−0.7	0.3	0.1
Aug	0.0	−0.8	−0.1	−0.4	0.6	0.7	1.4	**2.1**	0.5
Sep	__−2.2__	−0.8	−1.9	−1.3	−0.6	−1.3	−0.5	0.0	0.2
Oct	1.3	0.6	0.5	0.6	−1.4	0.1	−0.6	−0.3	−0.9
Nov	−0.8	−1.0	−0.9	−1.3	−1.5	−0.8	__−2.1__	__−2.0__	−0.9
Dec	0.0	−0.3	0.0	−0.3	−0.5	0.0	−0.3	−0.2	−0.3

Note: 1) GY-Guyuan, PL-Pingliang, HX-Huangxian, XF-Xifeng, CW-Changwu, WQ-Wuqi, WG-Wugong, XA-Xi'an, and TC-Tongchuan; 2) the underlined bold datum denote significant decreasing trends; and 3) the boxed bold datum represent significant increasing trends.
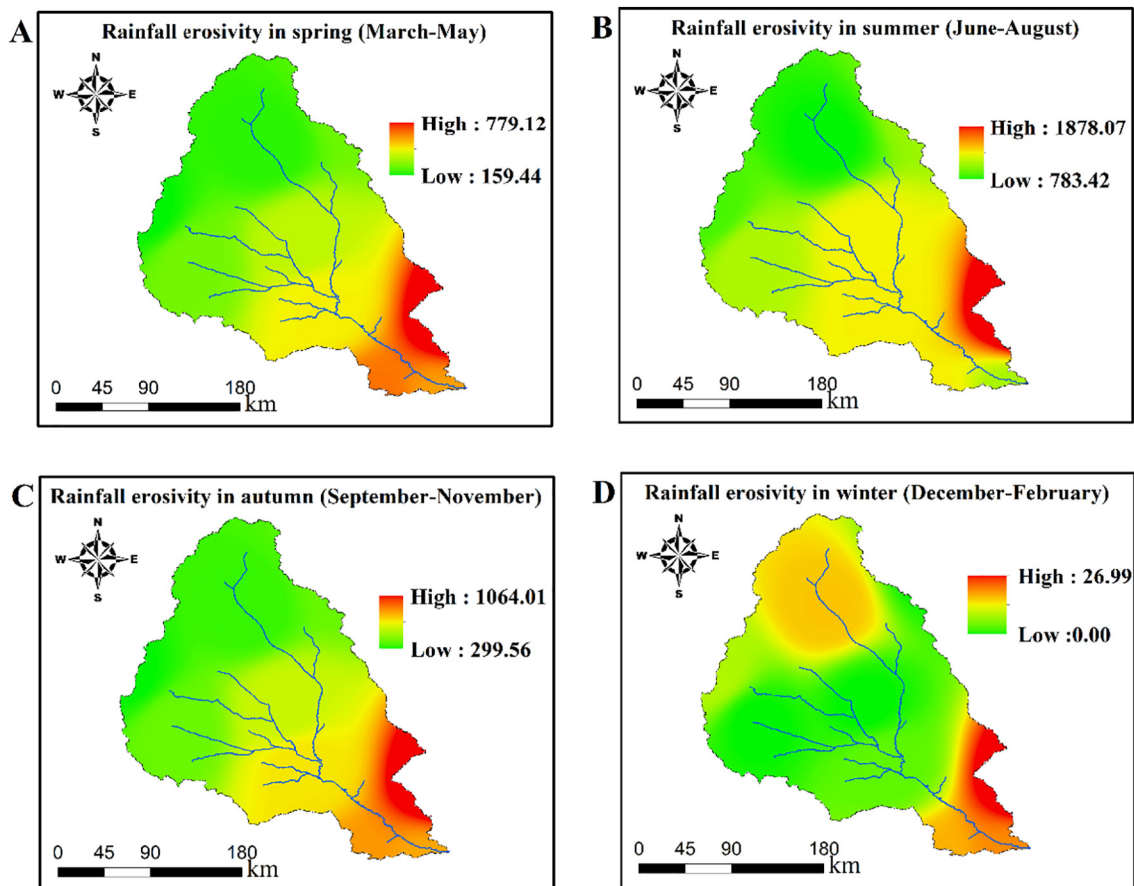
Fig. 3. Spatial distribution of seasonal mean rainfall erosivity (unit: MJ·mm·ha^{-1}·h^{-1}) in the JRB.
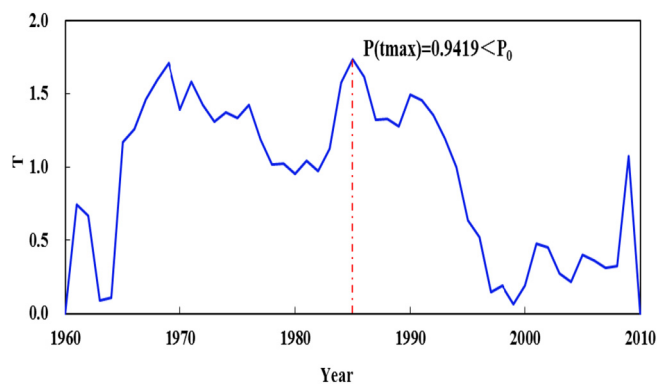

Fig. 4. Segmentation and change point of rainfall erosivity in the JRB. The blue line refer to the iteration and segmentation process. Since P(t_{max}) is smaller than the threshold of $P_0 = 0.95$, the segmentation process stops. (For interpretation of the references to color in this figure legend, the reader is referred to the web version of this article.)

segmentations and change points of annual rainfall erosivity in the JRB. It can be seen from Fig. 4 that the maximum value of T occurred in 1985, with corresponding $P(t_{max})$ up to 0.94 which is slightly less than P_0 (0.95). This indicates that the year of 1985 was a turning point in annual rainfall erosivity time series (1960–2010) in the JRB. Annual average rainfall erosivity (2018 MJ·mm·ha^{-1}·h^{-1}) during the period 1986–2010 was 9% less than that (2214 MJ·mm·ha^{-1}·h^{-1}) during the period 1960–1985. Similarly, the corresponding annual rainfall amount (519 mm) between 1986 and 2010 has reduced by 9% compared with that (571 mm) between 1960 and 1985. It is worth noting that annual rainfall erosivity time series is expected to be unstable due to the

decreasing annual rainfall amount. Therefore, it is of great importance to examine the possible causes of the changing rainfall erosivity.

4.2. Causes of rainfall erosivity variation

4.2.1. Relationship between rainfall and rainfall erosivity

Annual rainfall in the JRB has exhibited distinct temporal and spatial patterns as shown in Fig. 2B. According to the MMK trend test, there was a dominant but non-significant decreasing trend of rainfall with $-1.96 <$ all MMK values < 0 at the 95% confidence level. As for spatial distribution patterns, the highest rainfall was found in the downstream of the JRB, while the lowest rainfall was observed in the upstream of the JRB (Fig. 2B), which is highly consistent with the spatial pattern of annual rainfall erosivity (Fig. 2A). The consistency between annual rainfall and rainfall erosivity in terms of temporal and spatial patterns suggests that they are closely related (Fig. 2A and B).

To further reveal the relationship between rainfall and rainfall erosivity in the JRB, the scatter diagram and the cross wavelet power spectrum are shown in Fig. 5. The main information from the cross wavelet power spectrum diagrams in Fig. 5(B) are as follows: 1) the influencing cone of wavelet, namely the area surrounded by the fine arc, is set to avoid the boundary effect and the false information outside the cone; 2) the area surrounded by the thick real line denotes the cross wavelet power spectrum passing the test of standard spectrum of red noise at the 95% confidence level; 3) the numbers on the right of the color bar represent the relative power spectrum values; and 4) the arrow represents the phase relationship between factor 1 (like rainfall) and factor 2 (like rainfall erosivity). Particularly, the arrow "→" denotes that the variations of factor 2 and 1 are synchronous; "↓" indicates that the variation of factor 2 lags behind that of factor 1 with one fourth of resonant period (RP); "←" implies that the variation of factor 2 lags
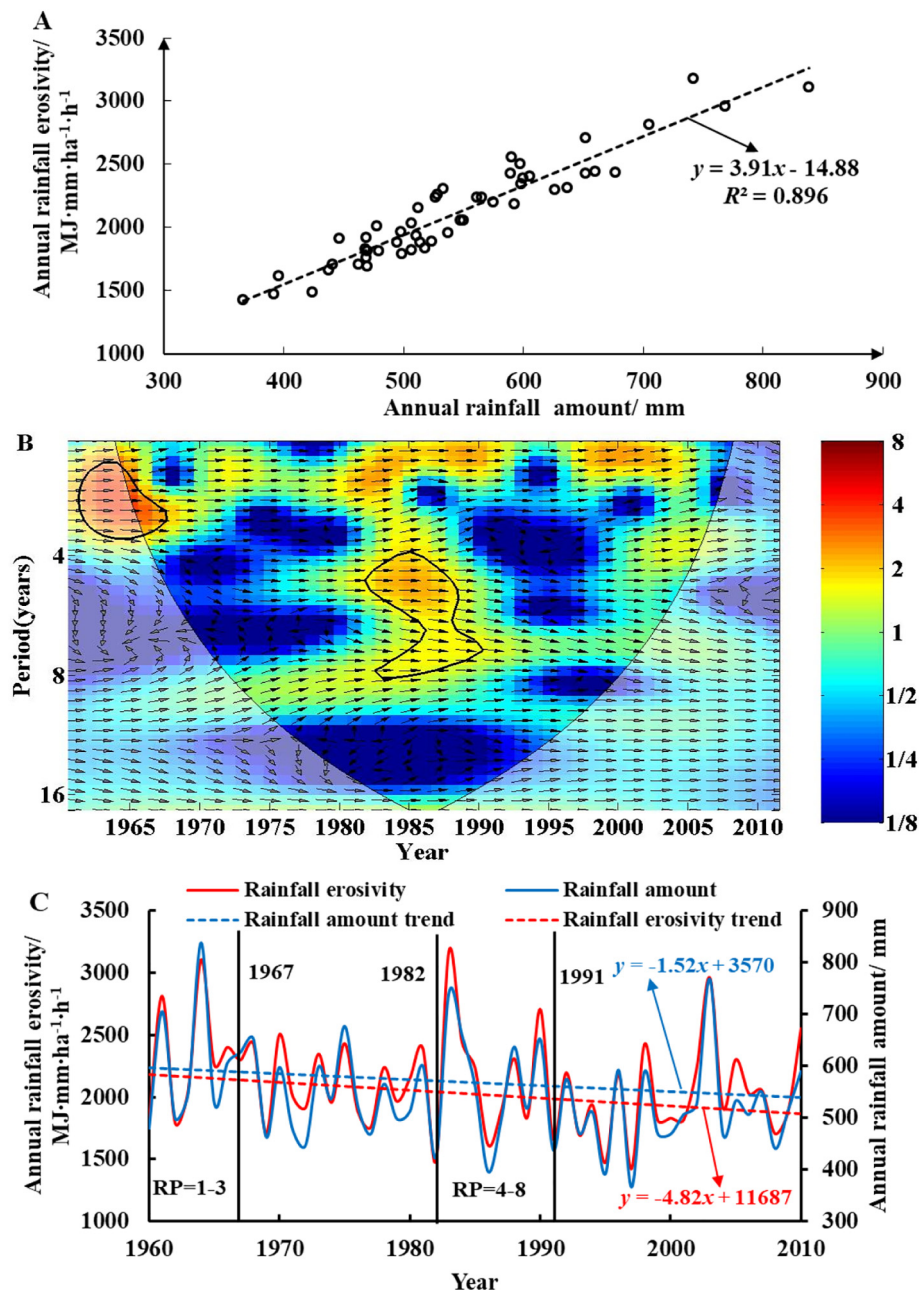
Fig. 5. The relationship between annual rainfall and erosive rainfall in the JRB: (A) scatter diagram; (B) cross wavelet power spectrum; and (C) variation processes.

behind that of factor 1 with a half RP; and "↑" shows that the variation of factor 2 lags behind that of factor 1 with three fourths of RP (Shao, 2013).

As shown in Fig. 5 A, there is an obvious linear positive relationship between annual rainfall amount and annual rainfall erosivity. Annual rainfall erosivity has increased by 3.9 MJ·mm·ha^{-1}·h^{-1} while annual rainfall amount increased by 1 mm. This suggests that annual rainfall erosivity changes were more dramatical than the annual amount in the JRB. Fig. 5B shows that rainfall erosivity and rainfall amount were positively correlated in the JRB. Especially, annual rainfall erosivity has showed a statistically significant positive correlation with annual rainfall variation with a 1–3 years' RP in 1960–1967 and a 4–8 years' RP in 1982–1991. Overall, annual rainfall erosivity has synchronously changed with annual rainfall amount in 1960–1967 and 1982–1991. Additionally, Fig. 5(c) shows that annual rainfall amount has exhibited a weak decreasing trend (−1.5 mm·a^{-1}), leading to an insignificant decreasing trend of rainfall erosivity (−4.8 MJ·mm·ha^{-1}·h^{-1}·a^{-1}) in the JRB.

4.2.2. Correlations between ENSO events/PDO and rainfall erosivity

Both ENSO events and PDO, partly reflecting global climate change, have strong impacts on rainfall in different regions around the world. Since rainfall and rainfall erosivity are closely linked (as outlined in Section 4.2.1), investigation of the detailed linkages between them and rainfall erosivity would help explore the remote causes of rainfall erosivity variation in a specific area, which is important for local rainfall erosivity prediction and adaptations. Here, the cross wavelet analysis was applied to explore the connections between ENSO events/PDO and rainfall erosivity in the JRB.

Fig. 6A displays the cross wavelet transform between the ENSO events and rainfall erosivity in the JRB. ENSO events have exhibited statistically negative correlations with rainfall erosivity with a 3 years' RP in 1967–1970. Besides, ENSO events and rainfall erosivity have showed a 3–6 years' RP in 1982–1991 when the variation of rainfall erosivity lags behind that of ENSO events with 1–2 years (Fig.6B). Note that the detected change point (i.e. the year 1985) in rainfall erosivity is
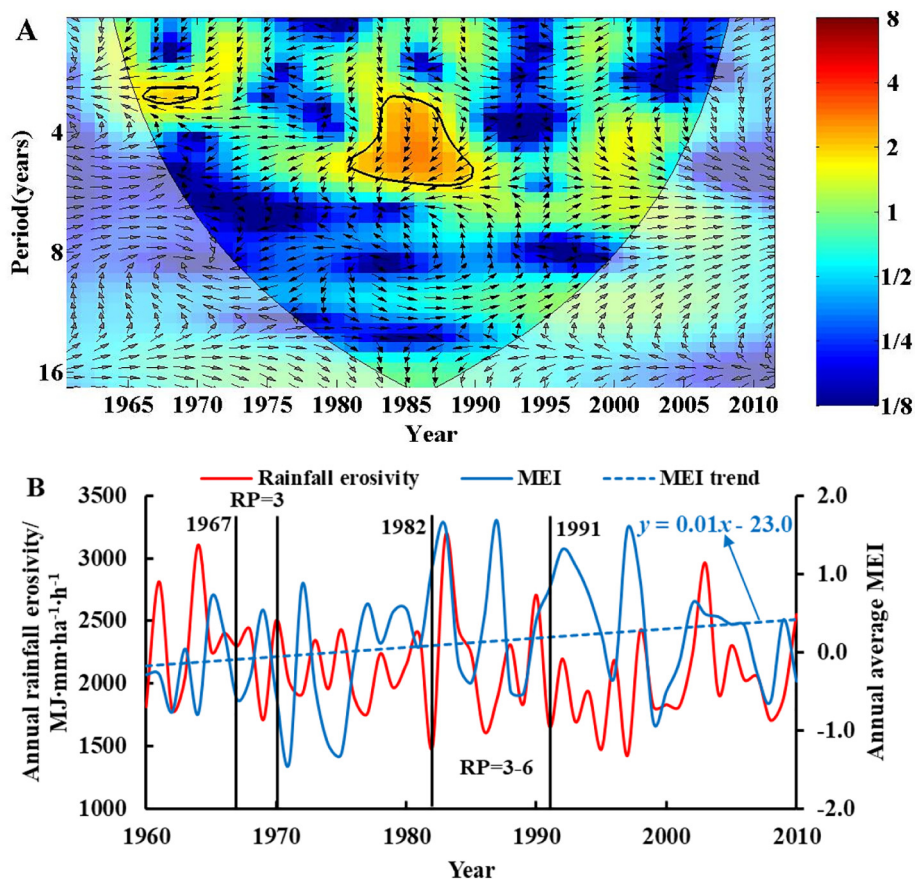
Fig. 6. The Relationship between annual average MEI and annual rainfall erosivity (A is the cross wavelet power spectrum; and B reflects the variation processes of MEI and rainfall erosivity).

consistent with the period of 1982–1991 when ENSO events showed strong correlations with rainfall erosivity. This finding suggests that ENSO events may have played important roles in the variation of rainfall erosivity in the JRB.

Similarly, Fig. 7A exhibits the cross wavelet transform between PDO and rainfall erosivity in the JRB. A significant positive relation was found between PDO and rainfall erosivity in the JRB with a 1–4 years' RP in 1982–1986, while a negative relation with a 4–6 years' RP in 1984–1992 was observed (Fig. 7B). It should be noted that the year of 1985 which is the turning point in rainfall erosivity in the JRB also lies in the period of 1982–1991 when PDO has showed strong correlations with rainfall erosivity.

Being different from ENSO events, PDO is a long-lasting El Niño-like pattern of Pacific climate variability. There are only two full PDO cycles in the past century: cool PDO phase during 1890–1924 and 1947–1976, and warm PDO regimes during 1925–1946 and 1977–1990s (Limsakul and Singhruck, 2016). PDO and rainfall erosivity correlated with each other during the 1980s–1990s, implying PDO warm phase was closely associated with the changing patterns of rainfall erosivity in the JRB.

Based on Figs. 6 and 7, it is evident that both PDO and ENSO events have had statistically significant correlations with rainfall erosivity in the JRB during 1982–1990, indicating that rainfall erosivity in the JRB has been the subject to the influence of PDO warm phase and ENSO events.

4.3. Implications of changing rainfall erosivity on sediment load and vegetation cover

4.3.1. Effects of rainfall erosivity on sediment load

Annual average sediment transported into the JRB is approximately 2.1×10^8 t during 1960–2010. According to the trend test, there was a significant decreasing trend of sediment discharge at the 95% confidence level with MMK statistic of −2.2. Fig. 8A shows the cross wavelet transform between rainfall erosivity and sediment load. Rainfall erosivity has showed statistically positive correlations with sediment discharge variations in the JRB with a 1–2 years' RP in 1963–1966, implying that rainfall erosivity was closely associated with sediment load in the JRB. Thus, the observed decreasing rainfall erosivity may have led to a reduction of sediment load in the JRB to a certain extent.

Human activities including water withdrawals and water and soil conservation practices may have affected the relationship between rainfall erosivity and sediment load in the JRB during 1960–2010, when sediment load had a significant decreasing trend while the rainfall erosivity had an insignificant decreasing trend. With development of economy after the reform and opening-up policy, large amounts of uncultivated lands were transformed into cropland equipped with irrigation. The irrigated areas in the WRB are approximately 9500 km² according to the census data from the Ministry of Water Resources, with large amounts of water diverted from the JRB and WRB. Reduced runoff in the river lowered the sediment carrying capacity, which further led to the decrease of sediment load (Wang et al., 2017).

Since soil loss is a serious problem in the JRB and WRB, great efforts have been made to carry out the measures of water conservation and ecological reconstructions (Sun et al., 2013; Huang et al., 2016a). The total areas experiencing different soil conservation practices in the WRB are displayed in the Table 3 (Huang et al., 2016a). Table 3 shows a small soil conservation area of 552 km² in 1960, indicating that impacts of human activities on sediment load are relatively weak. Thus, rainfall erosivity showed statistically positive correlations with sediment discharge variations in the JRB in 1963–1966. However, the soil conservation area has expanded tens-fold during the past decades, reaching to 33,344 km² in 2006, which has effectively reduced the vulnerability
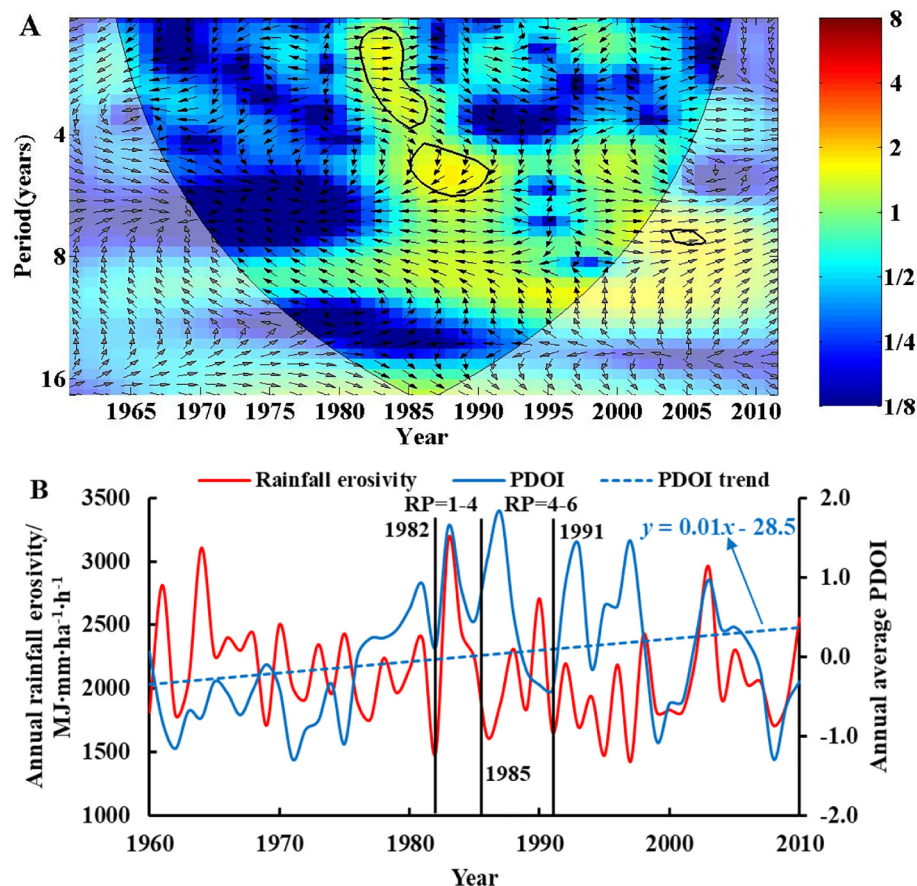
Fig. 7. The Relationship between annual average PDOI and annual rainfall erosivity (A is the cross wavelet power spectrum; and B reflects the variation processes of PDOI and rainfall erosivity).

to soil erosion, and resulted in a decrease in sediment load in river. Therefore, it can be concluded that human activities have altered the relationship between rainfall erosivity and sediment load in the JRB since 1970, which could be responsible for the decreasing sediment discharge of the basin (Wang et al., 2017).

4.3.2. Effects of rainfall erosivity on vegetation cover

Rainfall variability can affect soil water content and vegetation growth, with subsequent impacts on soil erosion (Sun et al., 2013). Previous studies have investigated the influence of rainfall magnitude on vegetation coverage, with little attention paid to the effects of rainfall erosivity (ChamailléJammes and Fritz, 2009; He, 2014).

Here, the vegetation coverage of the JRB as indicated by NDVI has exhibited a significant increasing trend at the 95% confidence level with MMK statistic of 3.25 during 1982–2010. Fig. 8B displays the cross wavelet transform between NDVI and rainfall erosivity in the JRB. No obvious correlations were observed between rainfall erosivity and NDVI, implying that other factors such as rainfall amount may be the major reason behind the variation of vegetation coverage in the JRB rather than rainfall erosivity. To investigate the relationship between rainfall amount and NDVI, the cross wavelet transform between NDVI and rainfall amount was repeated (Fig. 8C), which revealed a non-significant correlation between annual rainfall amount and NDVI as well. Overall, according to the cross wavelet analysis, both rainfall and rainfall erosivity were not related to the variation of NDVI in the JRB. But these results do not suggest that rainfall is not important for the vegetation development in the JRB. In fact, the relationship between NDVI and rainfall in the Loess Plateau is rather complicated and uncertain due to their complex interactions and other factors such as temperature and solar radiation which can influence NDVI variations

(Chen et al., 2008; Qi et al., 2009; Sun et al., 2013). Local soil types and attributes, elevation, land situation, vegetation types, annual precipitation distribution and other factors are expected to mask the real relationship between them (Qi et al., 2009), which should be addressed in a future study.

5. Conclusions

Soil erosion by water is a major environmental problem, especially in the Loess Plateau in China, which is well-known for its high erosion rate. In this study, we focused on rainfall erosivity, a key factor influencing soil erosion by water, in the JRB of the Loess Plateau. Spatial-temporal change patterns of rainfall erosivity were firstly examined, followed by a detailed investigation of, the underlying causes by exploring the linkages between rainfall erosivity and annual rainfall/ large-scale atmospheric circulation patterns. The impacts of the changing rainfall erosivity on sediment load and NDVI were also explored.

Generally, rainfall erosivity at the annual scale has showed insignificant decreasing trends with distinct spatial pattern across the JRB, and its stationarity didn't hold due to the decreasing rainfall. Interannual rainfall erosivity fluctuated markedly with significant increasing trend detected in summer in the eastern basin. Seasonal mean rainfall erosivity showed a spatial gradient with decrease from the upper to the lower stream of the JRB, and the largest rainfall erosivity in summer season.

Decreasing annual rainfall erosivity was linked with the reduction of rainfall amount (local climatic factor) in the JRB. Furthermore, both ENSO events and PDO warm phase (global climatic factors) have exerted significant impacts on rainfall erosivity during 1982–1991, consistent with the detected turning point (i.e. the year 1985) in annual
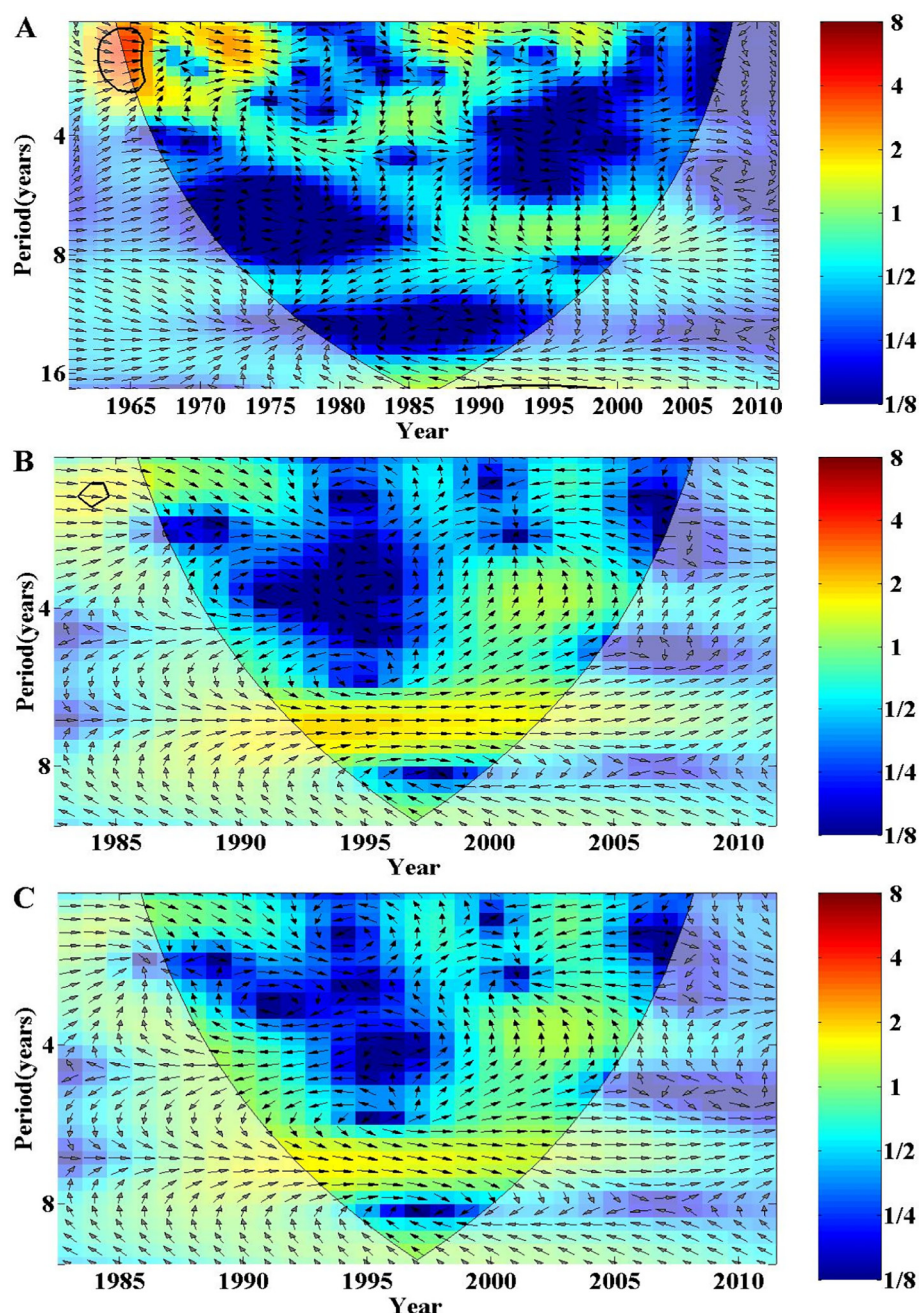
Fig. 8. The cross wavelet transforms between rainfall erosivity and sediment load (A), between rainfall erosivity and NDVI (B), and between rainfall amount and NDVI in the JRB.

Table 3
Areas of soil conservation practices in the WRB.

Year	Area of different soil conservation practice (km²)				Total(km²)
	Level terraces	Check dams	Grass-planting	afforestation	
1960	172	6	47	327	552
1970	974	24	193	1309	2500
1980	2918	64	446	3886	7314
1990	4758	78	2320	8468	15,624
2000	9088	134	3648	14,924	27,794
2006	11,779	143	4265	17,157	33,344

rainfall erosivity series. This implies that ENSO and PDO are remote drivers of the variation of rainfall erosivity in the JRB and could be used as input factors for local soil erosion prediction model.

Rainfall erosivity and sediment discharge were positively correlated in the early 1960s, but showed insignificant relations after the 1970s, partly due to the enhancement of human actives such as water withdrawals and soil conservation practices. Since rainfall erosivity was closely related to sediment load, it can be used as an input factor for the prediction of sediment discharge in the basin.

No significant correlation was found between rainfall erosivity and NDVI in the JRB. This could be attributed to the fact that the relationship between NDVI and rainfall in the Loess Plateau is rather complicated and uncertain due to their complex interactions and the influence of other factors such as temperature and solar radiation, which should be addressed in a future study.

Our results highlight the changing rainfall erosivity in the study region and the underlying local-scale and large-scale mechanisms, which have great implications for local soil erosion control and predictions.

References

Angulo-Martínez, M., Beguería, S., 2009. Estimating rainfall erosivity from daily precipitation records: a comparison among methods using data from the Ebro basin (NE Spain). J. Hydrol. 379 (1), 111–121.

Angulo-Martínez, M., Beguería, S., 2012. Do atmospheric teleconnection patterns influence rainfall erosivity? A study of NAO, MO and WEMO in NE Spain, 1955–2006. J. Hydrol. 450–451 (2), 168–179.

Ballabio, C., Borrelli, P., Spinoni, J., et al., 2017. Mapping monthly rainfall erosivity in Europe. Sci. Total Environ. 579, 1298–1315.

Bernaola-Galván, P., Ivanov, P.Ch., Amaral, L.A.N., Stanley, H.E., 2001. Phys. Rev. Lett. 87 (168105).

Bonilla, C.A., Vidal, K.L., 2011. Rainfall erosivity in central Chile. J. Hydrol. 410 (410), 126–133.

Borrelli, P., Diodato, N., Panagos, P., 2016. Rainfall erosivity in Italy: a national scale spatio-temporal assessment. Int. J. Digital Earth 9 (9), 835–850.

ChamailléJammes, S., Fritz, H., 2009. Precipitation-NDVI relationships in eastern and southern African savannas vary along a precipitation gradient. Int. J. Remote Sens. 30 (13), 3409–3422.

Chen, C.C., Xie, G.D., Zhen, L., et al., 2008. Analysis of Jinghe watershed vegetation dynamics and evaluation of its relation to precipitation. Chin. J. Ecol. 28 (3), 925–938 (in Chinese with English abstract).

Croitoru, A.E., Piticar, A., Burada, D.C., 2015. Changes in precipitation extremes in Romania. Quat. Int. 415, 1–11.

Daufresne, M., Lengfellner, K., Sommer, U., 2009. Global warming benefits the small in aquatic ecosystems. In: Proceedings of the National Academy of Sciences USA. Vol. 106 (31). pp. 12788–12793.

Djebou, D.C.S., Singh, V.P., Frauenfeld, O.W., 2015. Vegetation response to precipitation across the aridity gradient of the southwestern United States. J. Arid Environ. 115 (6), 35–43.

Fang, W., Huang, Q., Huang, S.Z., et al., 2017. Optimal sizing of utility-scale photovoltaic power generation complementarily operating with hydropower: a case study of the World's largest hydro-photovoltaic plant. Energy Convers. Manag. 136, 161–172.

Fang, W., Huang, S.Z., Huang, Q., et al., 2018. Reference evapotranspiration forecasting based on local meteorological and global climate information screened by partial mutual information. J. Hydrol (in press).

Gu, Z., Duan, X., Liu, B., et al., 2016. The spatial distribution and temporal variation of rainfall erosivity in the Yunnan plateau, Southwest China: 1960–2012. Catena 145, 291–300.

Hamed, K.H., Rao, A.R., 1998. A modified Mann–Kendall trend test for autocorrelated data. J. Hydrol. 204 (1–4), 182–196.

He, Y., 2014. The effect of precipitation on vegetation cover over three landscape units in a protected semi-arid grassland: temporal dynamics and suitable climatic index. J. Arid Environ. 109 (5), 74–82.

Hoyos, N., Waylen, P.R., Jaramillo, Álvaro, 2005. Seasonal and spatial patterns of erosivity in a tropical watershed of the Colombian Andes. J. Hydrol. 314 (1–4), 177–191.

Huang, S., Chang, J., Huang, Q., et al., 2014. Spatio-temporal changes in potential evaporation based on entropy across the Wei river basin. Water Resour. Manag. 28 (13), 4599–4613.

Huang, S., Huang, Q., Chang, J., et al., 2015a. Drought structure based on a nonparametric multivariate standardized drought index across the Yellow River basin, China. J. Hydrol. 530, 127–136.

Huang, S., Chang, J., Leng, G., Huang, Q., 2015b. Integrated index for drought assessment based on variable fuzzy set theory: a case study in the Yellow River basin, China. J. Hydrol. 527, 608–618.

Huang, S., Chang, J., Huang, Q., et al., 2016a. Quantifying the relative contribution of climate and human impacts on runoff change based on the Budyko hypothesis and SVM model. Water Resour. Manag. 30 (7), 2377–2390.

Huang, S., Huang, Q., Chang, J.X., et al., 2016b. Linkages between hydrological drought, climate indices and human activities: a case study in the Columbia River basin. Int. J. Climatol. 36 (1), 280–290.

Huang, S., Huang, Q., Leng, G.Y., et al., 2016c. A hybrid index for characterizing drought based on a nonparametric kernel estimator. J. Appl. Meteorol. Climatol. 55 (6), 1377–1389.

Huang, S., Ma, L., Chang, J., et al., 2018. Drought structure change characteristic across China based on an integrated drought index. J. Hydrol (in press).

Hudgins, L., Friehe, C.A., Mayer, M.E., 1993. Wavelet transforms and atmospheric turbulence. Phys. Rev. Lett. 71, 3279–3282.

IPCC, 2013. Summary for policymakers. In: Stocker, T.F., Qin, D., Plattner, G.-K., Tignor, M., Allen, S.K., Boschung, J., Nauels, A., Xia, Y., Bex, V., Midgley, P.M.E. (Eds.), Climate Change 2013: The Physical Science Basis. Contribution of Working Group I to the Fifth Assessment Report of the Intergovernmental Panel on Climate Change.

Jebari, S., Berndtsson, R., Olsson, J., et al., 2012. Soil erosion estimation based on rainfall disaggregation. J. Hydrol. 436–437, 102–110.

Kendall, M.G., 1955. Rank Correlation Methods. Griffin, London.

Labat, D., 2010. Cross wavelet analyses of annual continental freshwater discharge and selected climate indices. J. Hydrol. 385 (1), 269–278.

Lee, J.H., Heo, J.H., 2011. Evaluation of estimation methods for rainfall erosivity based on annual precipitation in Korea. J. Hydrol. 409 (1–2), 30–48.

Li, Z., Yan, F.L., Fan, X.T., 2003. The variability of NDVI over Northwest China and its relation to temperature and precipitation. In: Geoscience and Remote Sensing Symposium, 2003. IGARSS '03. Proceedings. 2003 IEEE International. Vol. 4. pp. 2275–2277.

Li, Z., Liu, W.Z., Zhang, X.C., et al., 2009. Impacts of land use change and climate variability on hydrology in an agricultural catchment on the loess plateau of China. J. Hydrol. 377 (1–2), 35–42.

Limsakul, A., Singhruck, P., 2016. Long-term trends and variability of total and extreme precipitation in Thailand. Atmos. Res. 169, 301–317.

Liu, S.Y., Huang, S.Z., Huang, Q., et al., 2017. Identification of the non-stationarity of extreme precipitation events and correlations with large-scale ocean-atmospheric circulation patterns: a case study in the Wei River Basin, China. J. Hydrol. 548, 184–195.

Liu, S.Y., Huang, S.Z., Huang, Q., et al., 2018. Spatial-temporal changes of maximum and minimum temperatures in the Wei River basin, China: changing patterns, causes and implications. Atmos. Res. 204, 1–11.

Mann, H.B., 1945. Nonparametric tests against trend. Econometrica 13, 245–259.

Maracchi, G., Sirotenko, O., Bindi, M., 2005. Impacts of present and future climate variability on agriculture and forestry in the temperate regions: Europe. Clim. Chang. 70 (1), 117–135.

Mello, C.R.D., Viola, M.R., Owens, P.R., et al., 2015. Interpolation methods for improving the RUSLE R-factor mapping in Brazil. J. Soil Water Conserv. 70 (3), 182–197.

Oliveira, P.T.S., Wendland, E., Nearing, M.A., 2012. Rainfall erosivity in Brazil: a review. Catena 100 (2), 139–147.

Panagos, P., Ballabio, C., Borrelli, P., et al., 2015. Rainfall erosivity in Europe. Sci. Total Environ. 511, 801–814.

Qin, W., Guo, Q., Zuo, C., et al., 2016. Spatial distribution and temporal trends of rainfall erosivity in mainland China for 1951–2010. Catena 147, 177–186.

Qi, Q., Wang, T.M., Kou, X.J., et al., 2009. Temporal and spatial changes of vegetation cover and the relationship with precipitation in Jinghe watershed of China. Chin. J. Plant Ecol. 33 (2), 246–253 (in Chinese with English abstract).

Ramos, M.C., Durán, B., 2014. Assessment of rainfall erosivity and its spatial and temporal variabilities: case study of the Penedès area (NE Spain). Catena 123, 135–147.

Renard, K.G., Foster, R., Weesies, G., et al., 1997. Predicting Rainfall Erosion by Water: A Guide to Conservation Planning with the Revised Universal Soil Loss Equation (RUSLE). In: USDA Agriculture Handbook. 703. pp. 1–367.

Santos, C.A.C.D., Neale, C.M.U., Rao, T.V.R., et al., 2011. Trends in indices for extremes in daily temperature and precipitation over Utah, USA. Int. J. Climatol. 31 (12), 1813–1822.

Shao, J., 2013. Multi-scale correlation analysis of hydrological time series based on cross wavelet transform. J. Hydroelectric Eng. 32 (2), 22–26 (in Chinese).

Sun, W., Shao, Q., Liu, J., 2013. Soil erosion and its response to the changes of precipitation and vegetation cover on the loess plateau. J. Geogr. Sci. 23 (6), 1091–1106.

Torrence, C., Compo, G.P., 2010. A practical guide to wavelet analysis. Bull. Am. Meteorol. Soc. 79, 61–78.

Trenberth, K.E., 2011. Changes in precipitation with climate change. Clim. Res. 47 (1), 123–138.

Vrieling, A., Sterk, G., De Jong, S.M., 2010. Satellite-based estimation of rainfall erosivity for Africa. J. Hydrol. 395 (3–4), 235–241.

Wang, S., Fu, B., Liang, W., et al., 2017. Driving forces of changes in the water and sediment relationship in the yellow river. Sci. Total Environ. 576, 453–461.

Wei, W., Chen, L., Fu, B., et al., 2007. The effect of land uses and rainfall regimes on runoff and soil erosion in the semi-arid loess hilly area, China. J. Hydrol. 335 (3–4), 247–258.

Wischmeier, B.W.H., Smith, D.D., 1978. Predicting rainfall erosion losses: a guide to conservation planning. In: Agricultural Handbook 537. USA Department of Agriculture.

Xin, Z., Yu, X., Li, Q., et al., 2011. Spatiotemporal variation in rainfall erosivity on the Chinese loess plateau during the period 1956–2008. Reg. Environ. Chang. 11 (1), 149–159.

Xie, Y., Yin, S.Q., Liu, B.Y., et al., 2016. Models for estimating daily rainfall erosivity in China. J. Hydrol. 535, 547–558.

Yang, F., Lu, C., 2015. Spatiotemporal variation and trends in rainfall erosivity in China's dryland region during 1961–2012. Catena 133, 362–372.

Yue, B.J., Shi, Z.H., Fang, N.F., 2014. Evaluation of rainfall erosivity and its temporal variation in the Yanhe River catchment of the Chinese loess plateau. Nat. Hazards 74 (2), 585–602.

Zhang, W.B., Xie, Y., Liu, B.Y., 2002. Rainfall erosivity estimation using daily rainfall amounts. Sci. Geogr. Sin. 705–711 (in Chinese with English abstract), 22.